# Astronomical Studies of Solar System Bodies 2060 Chiron and 1 Ceres

by

Jessica Dawn Ruprecht

Submitted to the Department of Earth, Atmospheric, and Planetary Sciences
in partial fulfillment of the requirements for the degree of

Master of Science in Earth and Planetary Sciences

at the

MASSACHUSETTS INSTITUTE OF TECHNOLOGY

June 2013





Author .....
Department of Earth, Atmospheric, and Planetary Sciences
May 22, 2013

Certified by .....
Richard P. Binzel
Professor of Planetary Sciences
Thesis Supervisor

Accepted by .....
Robert van der Hilst
Schlumberger Professor of Earth and Planetary Sciences
Head of Dept. of Earth, Atmospheric and Planetary Sciences

# Astronomical Studies of Solar System Bodies 2060 Chiron and 1 Ceres

by

Jessica Dawn Ruprecht

Submitted to the Department of Earth, Atmospheric, and Planetary Sciences
on May 17, 2013, in partial fulfillment of the
requirements for the degree of
Master of Science in Earth, Atmospheric, and Planetary Sciences

## Abstract

In this thesis two separate projects are investigated, a stellar occultation by 2060 Chiron and rotationally resolved spectra of 1 Ceres.

On 29 November 2011 UT, 2060 Chiron occulted a 14-mag star; data were successfully obtained at the 3-m IRTF on Mauna Kea and 2-m Faulkes North Telescope at Haleakala. The IRTF lightcurve shows a solid-body detection of Chiron's nucleus with a chord lasting $16.0 \pm 1.4$ seconds, corresponding to a chord length of $158 \pm 14$ km. Symmetric, dual extinction features in the Faulkes light curve indicate the presence of optically thick material roughly 300 km from the body midpoint. The duration of the features indicates a $\sim 3$ km feature separated by 10-14 km from a second $\sim 7$ km feature. The symmetry, optical thickness, and narrow size of these features allows for the intriguing possibility of a near-circular arc or shell of material.

Rotationally resolved spectra of Ceres in the 0.43-0.85 micron range were observed using the DeVeny spectrograph on the Perkins 72-inch telescope at Lowell Observatory. Spectral differences as a function of phase were investigated. It is concluded that Ceres' surface is uniform at the 1% level at visible wavelengths. Additionally, the 0.6 and 0.67 $\mu$m features reported by Vilas and McFadden [1992] and Fornasier et al. [1999] are not seen at any phase at the 1% level.

Thesis Supervisor: Richard P. Binzel
Title: Professor of Planetary Sciences

# Acknowledgments

I would like to thank Amanda Bosh, Rick Binzel, and Mike Person, who make up my thesis committee for their support and guidance in completing this work. I would also like to acknowledge the coauthors of the Chiron paper: Amanda Bosh, Mike Person, Federica Bianco, Amanda Gulbis, Schelte Bus, and Amanda Zangari. Additionally, thanks go to Dave Schleicher for his thoughts on the Chiron occultation results. I would also like to acknowledge Andy Rivkin, Stephen Levine, and Tom Bida for their aid and advice during the observing run and subsequent data analysis of the Ceres project. And last but not least, thanks go to Simone Agha for her efforts to improve the coherence of this work.

# Contents


**1 Introduction** **13**

**2 29 November 2011 Stellar Occultation by 2060 Chiron: Symmetric jet-like features** **17**

2.1 Photometric Studies and Evidence of a Coma . . . . . 17

2.2 Previous Occulation Studies . . . . . 17

2.3 Observation of a Stellar Occultation on 29 November 2011 UT . . . . 18

2.4 Data Reduction and Analysis . . . . . 20

2.5 Analysis of Light Curve Features . . . . . 22

2.5.1 Analysis of the IRTF MORIS Solid Body Detection . . . . . 22

2.5.2 Analysis of Symmetric Extinction Features . . . . . 23

2.6 Discussion . . . . . 25

2.7 Conclusions . . . . . 27

**3 Rotationally Resolved Spectra of 1 Ceres at Visible Wavelengths** **29**

3.1 Understanding Ceres Surface Mineralogy . . . . . 29

3.1.1 Possible Evidence for Hydrated Minerals at Visible Wavelengths 30

3.1.2 Variation in Surface Composition? . . . . . 30

3.2 Observation of 1 Ceres on 2-5 January 2013 (UT) . . . . . 31

3.3 Data Reduction . . . . . 33

3.3.1 Reducing the Effects of Fringing . . . . . 33

3.3.2 Extracting Spectra . . . . . 34

3.3.3 Parallactic Angle Effects . . . . . 34

3.3.4 Binning Spectra into Rotational Phase Bins . . . . . 36
3.4 Discussion . . . . . 37
3.4.1 Presence of the 0.6 and 0.67 $\mu$m Features . . . . . 37
3.4.2 Surface Variation . . . . . 38
3.5 Conclusions . . . . . 38

**4 Conclusions and Future Work** **41**

# List of Figures

2-1 This map shows a the trajectory of Chiron plotted on the Earth based on observed results. The trajectory uses the observed solid body detection of Chiron from the IRTF and assumes that the chord measured at the IRTF was central. . . . . 19

2-2 The complete light curve including all usable data from the 29 November 2011 observations at both the IRTF (blue) and Faulkes North Telescope (red). . . . . 21

2-3 A subset of the full light curve is plotted to better show detailed features near the occultation midpoint. The Faulkes North (red) data has been shifted forward by 7 seconds to account for the geographic offset between Faulkes and the IRTF (blue). Note the clear solid-body detection in the MORIS light curve, and the symmetric double extinction features in the Faulkes data. There is no solid body detection in the Faulkes lightcurve. . . . . 22

2-4 These plots show the regions nearest the extinction features seen in the Faulkes light curve. Left: features before the occultation midpoint. Right: features after the occultation midpoint. . . . . 24

2-5 Left: Comparison of MORIS light curve data with the Faulkes data after binning to 2 seconds. Binning produces features in the Faulkes data similar to those seen in the MORIS lightcurve. Right: The MORIS light curve is shown here folded over the occultation midpoint to test for the presence of symmetry in possible extinction features. Note the point of overlap apparent in the folded lightcurve. . . . . 25

3-1 This figure shows raw data frames of Ceres (top) and Hyades 64 (bottom) on the night of 4 January 2013 (UT). Note that wavelength decreases to the right (bluer). The slit was 2.4". Along the y-axis the target is surrounded by sky, and two sky emission lines are visible in the Ceres sky background. . . . . 32

3-2 The master flat for observations on 4 January 2013. Notice the substantial fringing effects in the red (left) end of the chip. . . . . 33

3-3 The complete set of calibrated Ceres spectra observed on the night of 5 January 2013. Each spectrum represents the average of 10 individual 90 second exposures. Airmass increases from left to right and from top to bottom. . . . . 35

3-4 Calibrated Ceres spectra in ten phase bins are plotted on the same axes with artificial offsets. An A-star spectrum (black) is included to help identify uncorrected telluric features. Vertical lines are used to denote the 0.6 and 0.67 $\mu$m wavelengths where features have been seen in previous studies. No significant absorption features are apparent in the phased Ceres spectra. . . . . 36

3-5 Ratios of spectra at different phase bins. Spectra have been trimmed to the 0.55-0.8 $\mu$m region to exclude the reddest and bluest regions which are most contaminated by fringing and parallactic angle effects. No evidence for additional features is seen. Top: Ratios of adjacent phase bins. Bottom: Ratios of opposite phases. . . . . 39

# List of Tables

2.1 Occultation prediction parameters. . . . . 19
2.2 Summary of Chiron occultation observations. . . . . 20
2.3 Summary of occultation data acquired. . . . . 20

3.1 Summary of data acquired during 2-5 January 2013 observations of Ceres. . . . . 33
3.2 Summary of spectral feature analysis. . . . . 37

# Chapter 1

# Introduction

Astronomy is one of the oldest fields of scientific inquiry, first undertaken by ancient civilizations thousands of years ago. Among the earliest discoveries of the first astronomers was that some objects in the sky moved differently than the rest of the stars. Today we know these objects to be the planets. Though it would take many more centuries to recognize that the Earth was itself a planet that orbits the Sun, the discovery of the planets represents the beginning of our understanding of the solar system. Despite centuries of work, astronomy today continues to yield new information about our solar system.

While the technology used for astronomy in the modern era has greatly improved the ability of astronomers to study objects in detail, the basic techniques for studying such objects remain largely unchanged. The basic measurements that astronomers make today involve observing changes in the brightness of objects (photometry), changes in the positions of objects (astrometry), and spectral measurements of the light from objects (spectroscopy). These fundamental techniques have been leveraged with exceptional success to learn about a great variety of astronomical phenomena. In this thesis, photometry is used to observe a stellar occultation and spectroscopy is used to study the composition of the largest main belt asteroid, 1 Ceres.

A stellar occultation occurs when an object within our solar system passes in front of a distant star and blocks all or some of the light from the star. By observing how the apparent brightness of the star changes as the object passes in front of it, these

observations can be used to learn about the object. Such observations can measure the size of the object, detect the presence of an atmosphere around it, and identify the presence of material bound gravitationally to the object such as satellites or rings.

2060 Chiron, the target of the occultation observed in this thesis, is an object of particular interest since it has been shown to exhibit cometary behavior even though it never comes much closer to the Sun than Saturn, whereas most comets exhibit very little coma or other cometary behavior at such distances. One possible explanation for this seemingly anomalous behavior lies in the possibility that Chiron may have formed in the Kuiper belt and since have had its orbit perturbed through gravitational interactions to shift it further in toward the Sun [Jewitt, 2009]. If this were the case, Chiron might be expected to have reserves of volatiles that are unstable at its current orbital radius, and the sublimation of these volatiles could explain why cometary behavior is observed even at large solar distances. 2060 Chiron was observed to determine basic properties of the body, such as its size and to investigate any evidence for cometary activity, such as coma or dust jets.

In spectroscopy, the light from an astronomical object is separated into its component wavelengths and variations in brightness as a function of wavelength are investigated. In this way emission and absorption features can be identified which provide information about the composition of the surface from which the light was emitted or reflected. Thus, by measuring spectra astronomers can learn about the surface composition of objects very far away.

When taking spectra of rocky objects within our solar system (such as asteroids), the light observed is sunlight reflected from the surface of the object. This creates a problem: the spectrum of the Sun and the spectrum of the rocky surface are intermingled because the light incident on the surface of the object already contains the inherent spectrum of the Sun. To counter this problem, it is necessary to take spectra of a star similar to the Sun or of the Sun itself and divide the asteroid spectrum by this solar-type spectrum. This division results in the asteroid spectrum without the contribution from the Sun and is called a reflectance spectrum. Additionally, the process of division by a solar reference spectrum helps to remove spectral features

inherent to the Earth's atmosphere. The reflectance spectrum can subsequently be used to investigate the compositional features inherent to the surface of the asteroid.

The target of this study, 1 Ceres is currently of particular interest because it is a target of the Dawn spacecraft, scheduled to arrive at Ceres in 2015. Rotationally resolved spectra of 1 Ceres were taken at visible wavelengths with the twin goals of resolving discrepancies regarding features seen in the visible wavelength spectrum and adding to the current understanding of Ceres's surface mineralogy by looking for possible evidence of compositional variations in the surface which can bee seen as it rotates.

Each chapter in this thesis presents one of these two projects and each was written as a stand-alone paper intended to be submitted for publication.

# Chapter 2

# 29 November 2011 Stellar Occultation by 2060 Chiron: Symmetric jet-like features

## 2.1 Photometric Studies and Evidence of a Coma

Photometric studies have demonstrated that Chiron is an active body exhibiting outbursts and periods of increased brightness on timescales from hours to years. Observations in 1988 and 1989 [Luu and Jewitt, 1990] demonstrated the development of a coma by comparing the annular surface brightness of Chiron between the two observations. Changes in flux on short timescales were observed in January 1990 when Chiron was observed to exhibit brightening during an 8 hour observation [Luu and Jewitt, 1990].

## 2.2 Previous Occultation Studies

A stellar occultation of Chiron observed from 5 sites in November 1993 [Bus et al., 1996] yielded a positive detection of the nucleus and a possible graze of the nucleus and put some of the first bounds on the size of Chiron. In the case of a positive nuclear graze, the radius was found to be $89.6 \pm 6.8$ km. Using just the solid-body detection,

the radius was constrained to be greater than $90.2 \pm 6.5$ km. Combining the 1993 data with new data from a March 1994 Chiron occultation [Elliot et al., 1995] yielded a radius constraint of 83-156 km. More recently, observations by Fernandez et al. [2002] have determined a radius of $74 \pm 4$ km using thermal models. This thermal result may suggest that Chiron's true size is more similar to the lower end of the stellar occultation measurements.

The 1993 and 1994 stellar occultation observations also provided evidence for cometary jet activity on Chiron in the form of narrow, low optical depth extinction features. The 1994 occultation identified a feature 5-9 km wide (FWHM) with optical depth $\tau \sim 0.92$, as well as evidence of several broader features. The narrow feature was determined to be due to jet-like activity rather than the result of a grazing nuclear occultation [Elliot et al., 1995]. Similar features with widths $< 30$ km and $\tau \sim 0.4 - 0.8$ were also identified in the 1993 occultation lightcurves and were again explained as narrow, collimated jets of material escaping from the nuclear surface [Bus et al., 1996].

## 2.3 Observation of a Stellar Occultation on 29 November 2011 UT

An occultation of Chiron with a 14.8-mag star (2UCAC 29938128) was observed on 29 November 2011 UT at the 3-m IRTF on Mauna Kea and the 2-m Faulkes North Telescope at Haleakala, part of the Las Cumbres Observatory Global Telescope Network (Figure 2-1, Table 2.1). Data on the IRTF were taken at optical wavelengths with MORIS (MIT Optical Rapid Imaging System) [Gulbis et al., 2010] and simultaneously in the 0.69-2.4 micron region using SpeX, a medium resolution 0.8-5.4 micron spectrograph [Rayner et al., 2003]. Data from the Faulkes North Telescope were taken only in the optical using LIHSP, an Andor iXon888 back-illuminated EMCCD. Observations using MORIS were taken at 2 second exposures, while at Faulkes data were taken with a 0.2 second cadence. Observations were made without a filter with

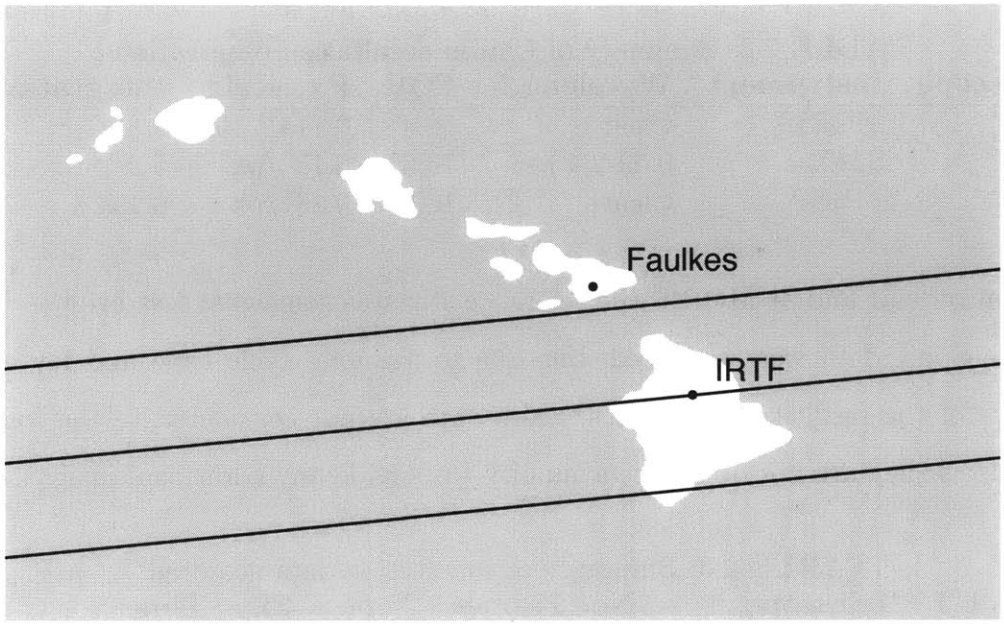


**FIGURE** 2-1: This map shows a the trajectory of Chiron plotted on the Earth based on observed results. The trajectory uses the observed solid body detection of Chiron from the IRTF and assumes that the chord measured at the IRTF was central.

MORIS and at Faulkes North to maximize the star signal given the short exposure times. Calibration data including dark, bias, and flat field frames were taken with MORIS but not at the Faulkes North Telescope (Tables 2.2, 2.3).

**TABLE** 2.1: Occultation prediction parameters.

| **Site** | **Midtime** | **Sky-plane Vel.** | **Close Approach** |
|---|---|---|---|
| IRTF | 08:15:36 UT | 9.87 km/s | 147 km N |
| Haleakala | 08:15:29 UT | 9.87 km/s | 244 km N |

Only the first 875 frames taken using MORIS were used in this analysis due to increasing cloud cover. The frames taken at Faulkes were not affected by clouds; however, after the occultation the reference star wandered out of the frame, making it impossible to perform relative photometry. Thus, only the first 4882 frames of the Faulkes data were analyzed.

In both the MORIS data and the Faulkes data only one on-chip reference star was available in the frame. At Faulkes, the reference star was brighter than the

**TABLE** 2.2: Summary of Chiron occultation observations.

| Telescope | Instrument | Wavelength | FOV | Px. scale | Integration | Cycle |
|---|---|---|---|---|---|---|
| IRTF | MORIS | Clear | 58.4" | 0.1141"/px | 2 s | 2 s |
| IRTF | SpeX | 0.69-2.4 $\mu$m | 76.8" | 0.15"/px | 5 s | 9.61 s |
| FNT | LIHSP | Clear | 169" | 0.33"/px | 0.194 s | 0.20074 s |

occultation star and at MORIS the reference star was somewhat less bright.

The SpeX data were analyzed, but due to the long cycle time and low signal-to-noise of the resulting lightcurves, these data are not considered in the following analysis as they are not of sufficient quality to provide any additional insight.

**TABLE** 2.3: Summary of occultation data acquired.

| Date UT | Telescope | No. Frames | Type | Exp. Time |
|---|---|---|---|---|
| 11/29 | IRTF (MORIS) | 1200 | Object | 2 s |
| 11/29 | IRTF (MORIS) | 100 | Bias | 0.28 s |
| 11/29 | IRTF (MORIS) | 100 | Dark | 2 s |
| 11/29 | IRTF (MORIS ) | 100 | Flat | 0.28 s |
| 11/29 | IRTF (SpeX) | 135 | Object | 5 s |
| 11/29 | IRTF (SpeX) | 3 | Argon | 0.18 s |
| 11/29 | Faulkes | 7500 | Object | 0.2 s |

## 2.4 Data Reduction and Analysis

To extract information about Chiron from the raw stellar occulation data frames, photometry was performed on the combined Chiron-star images, relative to the on-chip reference star. Only the IRTF MORIS data had appropriate calibration frames to allow for flattening of the data. The raw Faulkes data frames were used to generate the light curve since no calibration data were available; however, analysis of empty frames taken after the stars had wandered out of the field determined the background to be flat to within 1%. Optimal star and sky box sizes around both the occulted star and the reference star were chosen to maximize the SNR of the lightcurve.

The resulting lightcurves are plotted in Figure 2-2, where the baseline star flux from the occultation star has been normalized to one. In the MORIS lightcurve this was done by first subtracting the median solid-body detection value (assumed to be

the Chiron flux level) and then normalizing the upper baseline to unity.

In the Faulkes data there is no solid-body detection from which to measure the Chiron flux level; however, because the same star is observed in both frames, the percent of the flux contributed by Chiron should be the same in both raw photometry data from both Faulkes and MORIS. This is a reasonable assumption, given that both data sets were taken without a filter but may not be perfect due to possible differences in the mirror properties of the different telescopes. The percentage of flux due to Chiron at MORIS was calculated by taking the ratio of the flux at the solid body detection to the baseline flux level. The Faulkes baseline was then multiplied by this ratio and the result was subtracted from the Faulkes lightcurve to remove the Chiron flux from the final lightcurve. Only then was normalization of the upper baseline level to unity performed.

To account for the difference in longitude of the two sites the Faulkes data has been shifted forward by 7 seconds, based on the predicted offset in midtime, to align the occultation midpoint with that seen in the IRTF data (Table 2.1). A zoomed-in view detailing the features seen near the occultation midpoint is given in Figure 2-3.

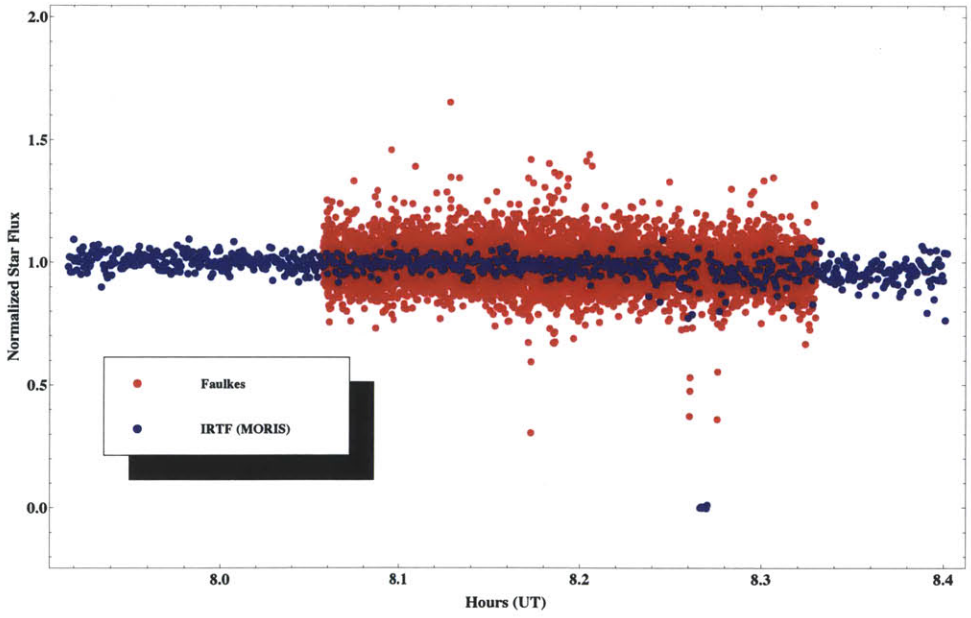


**FIGURE** 2-2: The complete light curve including all usable data from the 29 November 2011 observations at both the IRTF (blue) and Faulkes North Telescope (red).

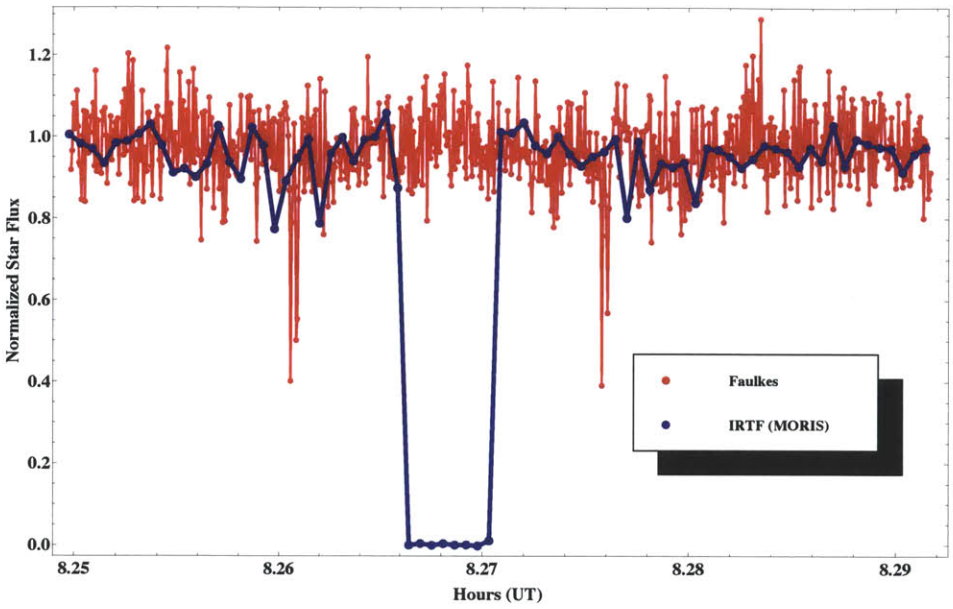


**FIGURE** 2-3: A subset of the full light curve is plotted to better show detailed features near the occultation midpoint. The Faulkes North (red) data has been shifted forward by 7 seconds to account for the geographic offset between Faulkes and the IRTF (blue). Note the clear solid-body detection in the MORIS light curve, and the symmetric double extinction features in the Faulkes data. There is no solid body detection in the Faulkes lightcurve.

## 2.5 Analysis of Light Curve Features

The lightcurves in Figures 2-2 and 2-3 reveal several features. Most obvious is the solid-body detection in the MORIS lightcurve where the flux from the star decreases for 8 frames. On either side of this detection are symmetric features in the Faulkes data which can be seen in Figure 2-3 to be a pair of narrow features. In these features, the flux decreases only to around 50% extinction. These shallower features are not considered evidence of a solid body detection because the flux does not go to zero and they are distant from the occultation midpoint without including it.

### 2.5.1 Analysis of the IRTF MORIS Solid Body Detection

The solid-body detection present in the IRTF MORIS data can be used to constrain the size of Chiron. The length of the drop in flux corresponds to a measurement of

the size of Chiron along a chord through the body and places a lower bound on the radius. In the IRTF data, the chord length is measured to be $16.0 \pm 1.4$ seconds. The sky plane velocity at the IRTF is calculated to be 9.87 km/s, implying a chord length of $158 \pm 14$ km. Assuming this chord is central places a lower bound on the size of Chiron of $79 \pm 7$ km.

Further assumptions about the geometries of Chiron and the telescopes can be used to convert the chord length into a range of possible radii. Assuming Chiron is spherical and that the path of the Faulkes North Telescope just grazes tangent to the nucleus, the chord length can be used to place an upper bound on the size of Chiron using

$$r = \sqrt{\frac{c^2}{4} + (r - h)^2} \tag{2.1}$$

where $r$ is the radius, $c$ is the chord length, and $h$ is the distance between the chord and the nucleus edge (equal to the IRTF-Faulkes distance perpendicular to the occultation path, 97 km). Solving for the radius using the extrema of the chord length yields a possible radius range for the Chiron nucleus of 75-87 km. Combining these two size estimates bounds the size of Chiron from 72-87 km, consistent with the lower limit of the previous occultations (83-156 km) [Elliot et al., 1995], as well as with the more recent thermal result ($74 \pm 4$ km) [Fernandez et al., 2002], and represents a significant refinement of the previous occultation results.

### 2.5.2 Analysis of Symmetric Extinction Features

The extinction features present in the Faulkes light curve are particularly interesting because of their apparent symmetry about the occultation midpoint and because the observed 40-60% extinction ($\tau = 0.7 - 1.0$) indicates that the features show nearly equal extinction depths. Note that the Chiron flux subtraction procedure performed in the analysis increases the depth of the extinction features by 2-3% and results in an increase in optical depth of 0.1 compared to basline normalization without prior Chiron flux removal.

Measurement of the full-width, half-minimum (FWHM) of the extinction features

in Figure 2-4 was performed by counting the number of points below half-min and multiplying by the exposure time and sky-plane velocity (Tables 2.1, 2.2). This analysis indicates that the spacing between the minima of the double features correspond to a distance of $12 \pm 2$ km. Using the FWHM, the extinction features before the occultation midpoint have widths: $4 \pm 2$ km and $6 \pm 2$ km. After the occultation midpoint the FWHM of the features is $3 \pm 2$ km and $7 \pm 2$ km. The distance of these features from the nucleus was estimated by comparing the separation between the Faulkes extinction features with the midpoint of the observed chord in the IRTF data, yielding a distance of $266 \pm 15$ km between the body center and the feature seen in the Faulkes lightcurve.

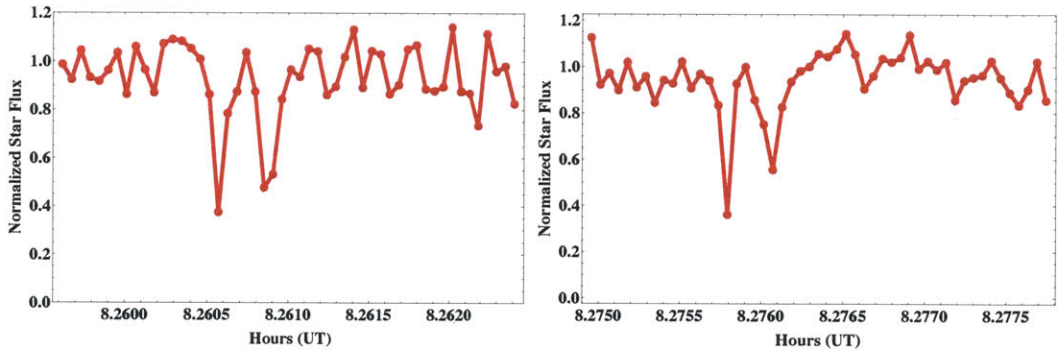


**FIGURE** 2-4: These plots show the regions nearest the extinction features seen in the Faulkes light curve. Left: features before the occultation midpoint. Right: features after the occultation midpoint.

If the Faulkes extinction features are evidence of a circularly symmetric structure around Chiron, it is expected that similar extinction features would be seen in the IRTF MORIS light curve. To test for such features, the Faulkes light curve was binned to 2 seconds (a spatial resolution of 20 km) to provide a comparison with the MORIS lightcurve (Figure 2-5). Binning reduces the contrast of the Faulkes features due to their narrow width, and results in features of similar depth to those in the MORIS lightcurve.

Because of the presence of features in the MORIS data that appear similar to the binned Faulkes lightcurve features, the IRTF lightcurve was then folded about the observed midtime to test for feature symmetry. The folded IRTF light curve

exhibits one clear point of overlap in a feature that is consistent with the binned Faulkes extinction features. The features seen in the MORIS data are farther from the nuclear center ($306 \pm 15$ km) than those seen in the Faulkes data. This supports the notion of a circular or near-circular geometry since chord lengths are shorter when measured at greater distances from the circle center.

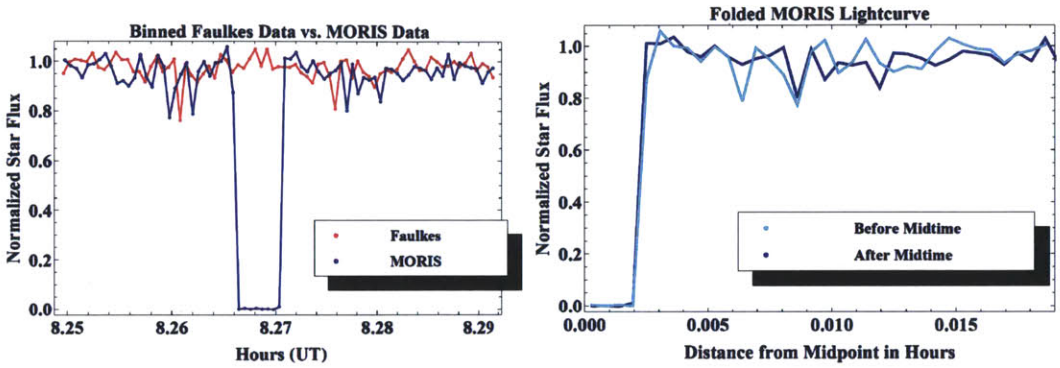


**FIGURE** 2-5: Left: Comparison of MORIS light curve data with the Faulkes data after binning to 2 seconds. Binning produces features in the Faulkes data similar to those seen in the MORIS lightcurve. Right: The MORIS light curve is shown here folded over the occultation midpoint to test for the presence of symmetry in possible extinction features. Note the point of overlap apparent in the folded lightcurve.

## 2.6 Discussion

The symmetric, narrow features seen in these observations are similar to those seen in previous Chiron occultation studies [Elliot et al., 1995, Bus et al., 1996]. In both of these occultations narrow features were observed within a few hundred kilometers of the nuclear surface. However, the features observed in this occultation and in previous Chiron occultations are much narrower than those generally observed in cometary studies.

The November 1993 Chiron occultation observed by Bus et al. [1996] provided evidence for a narrow feature $\sim$ 250 km from the nuclear surface and no wider than 22 km. The exposure times do not allow for the resolution of narrower features, such as those observed in 2011. In fact, it is likely that a double feature as narrow as the one observed in the 2011 Faulkes data would have appeared as a single feature in the

1993 event. In addition to this narrow jet feature, broad low-level fluctuations were observed in the Bus et al. [1996] occultation light curves. These broad features were attributed to the presence of a gravitationally bound coma.

The March 1994 occultation described in Elliot et al. [1995] similarly indicated the presence of a narrow jet feature with a width of $\sim$ 10 km and located $126 \pm 16$ km from the nuclear surface. A second possible jet was also observed, located $\sim$ 300 km from the body surface and with a width of $\sim$ 75 km, and it was suggested that these two features could represent detection of material from the same source forming a spiral or suborbital arch. The Elliot et al. [1995] occultation also observed a broad feature which was again attributed to the presence of a coma.

The narrow features detected in the two previous occultations are in many ways similar to the features seen in the 2011 event. Again, narrow features with total width less than 20 km are observed located hundreds of kilometers from the nuclear surface. The significant difference between the 2011 occulation and previous results lies in the symmetric detection of similar features on both sides of the nucleus.

Collimated jets of material have been observed in many cometary studies and are generally considered to have two formation mechanisms: gaseous sublimation from the nuclear surface or interactions between gas and dust flows in the coma, resulting in hydrodynamic shocks at flow boundaries [Farnham, 2009]. These collimated features are known to result in a variety of observed coma morphologies including fans, jets, arcs, shells, and spirals. The observed coma morphology varies strongly as a function of the direction of the rotation pole with respect to the sky plane of the observer and the location of the active sources [Schleicher and Farnham, 2004]. This information is poorly constrained for Chiron with significant uncertainty in the pole orientation [Fulle, 1994], making modeling of the observed occultation features impractical; however, due to the symmetry of the observed features, it is likely that the feature is the result of an arc or shell of dusty material expanding away from the nuclear surface produced by one or more active regions on the nuclear surface.

The presence of features 300 km from the surface of Chiron observed during the 2011 observation at a solar distance of nearly 17 AU, indicates the presence of activity

near aphelion. A simple calculation to estimate particle motion ejected at escape velocity demonstrates that travel time to 300 km from the nuclear surface is on the order of a few hours, indicating ongoing activity at the time of the occultation. This conclusion is further supported by numerical simulations which show that even at aphelion the median particle lifetime for small dust grains around Chiron is only 7 days [Stern et al., 1994]. The 1993 and 1994 occultations were observed when Chiron was approaching perihelion, at roughly 9 AU. Therefore, the observation of active cometary behavior similar to that seen in the 1993 and 1994 events could seem unusual given Chiron's distance from the sun in 2011; however, Chiron has been known to exhibit activity even at aphelion. Analysis of pre-discovery photographic plate data shows that Chiron exhibited a period of significant activity in the 1970s at a distance of 18 AU [Bus et al., 2001].

Chiron's history of activity near aphelion constrains the possible mechanisms contributing to the observed cometary behavior. Due to the extremely large solar distance at aphelion, the most common volatiles responsible for cometary behavior, $H_2O$ and $CO_2$ ices, must be excluded because they lack sufficient volatility at these distances to support the observed coma [Stern et al., 1994]. Instead the observed cometary behavior is more commonly attributed to highly volatile ices such as CO ice [Meech and Belton, 1990, Stern et al., 1994]; however, alternative mechanisms such as the crystallization of amorphous water ice containing volatile gases in the interior of Chiron have also been suggested [Prialnik et al., 1995].

## 2.7 Conclusions

On 29 November 2011 UT observation of a Chiron occultation yielded optical data from the 3-m IRTF with MORIS on Mauna Kea and the 2-m Faulkes North Telescope at Haleakala as well as spectral data in the $0.8-5.4$ $\mu$m range from SpeX at the IRTF. The presence of a solid-body detection in the IRTF MORIS light curve determines a chord length of $158 \pm 14$ km. By making some geometrical assumptions, the radius can be constrained to between 75-87 km, consistent with previous results in Elliot

et al. [1995] and Fernandez et al. [2002].

Timing analysis of the symmetrical extinction features present in the Faulkes and MORIS light curves indicates the presence of a symmetrical structure with nearly-circular geometry. The feature seen in the Faulkes lightcurve is a double feature consisting of a 3 km feature and a 7 km feature separated by a distance of 10-14 km. These extinction features are observed to be roughly 300 km from the nucleus, and are similar to features observed by previous stellar occultations [Elliot et al., 1995, Bus et al., 1996], which were interpreted to be the result of collimated dust jets ejecting material from the nuclear surface. Due to the symmetry of the observed features about the occultation midpoint, an interpretation such as an arc or shell of dusty material may be more plausible for the 2011 observations. The presence of these features in the 2011 occultation data indicate that Chiron was active at the time of the occultation.

# Chapter 3

# Rotationally Resolved Spectra of 1 Ceres at Visible Wavelengths

## 3.1 Understanding Ceres Surface Mineralogy

Early spectral studies of 1 Ceres [McCord and Gaffey, 1974, Chapman and Salisbury, 1973] attempted to identify the surface composition by comparing reflectance spectra with those of meteoritic samples. These early studies led to the conclusion that the surface composition of Ceres was most similar to carbonaceous chondrite meteorites, but that it was not a match to any known meteorite sample [McCord and Gaffey, 1974]. More recent spectral studies at visible wavelengths found possible evidence for hydrated iron-bearing phyllosilicates [Golubeva et al., 1983, Vilas and McFadden, 1992, Fornasier et al., 1999].

Studies in the 0.1-0.4 $\mu$m range provided stronger evidence for the presence of hydrated minerals on Ceres [Lebofsky, 1978, Lebofsky et al., 1981]. A strong absorption feature centered near 3 $\mu$m has been observed in multiple studies [Lebofsky, 1978, Lebofsky et al., 1981, King et al., 1992, Rivkin et al., 2006], and many possible explanations have been proposed, including water frost [Lebofsky et al., 1981] and ammonium-bearing phyllosilicates [King et al., 1992]. Most recently, Milliken and Rivkin [2009] showed that the 0.3 $\mu$m features were well modeled by brucite and Mg-bearing carbonates formed in the presence of $H_2O$ and $CO_2$.

### 3.1.1 Possible Evidence for Hydrated Minerals at Visible Wavelengths

An early study performed by Golubeva et al. [1983] identified a number of spectral features which were attributed to the presence of iron and nickel deposits in a silicate crystalline structure. Features at 0.39, 0.41, 0.54, 0.59, and 0.7 $\mu$m were identified. The 0.59 $\mu$m feature was attributed to the presence $Fe^{3+}$ ion and it was suggested that this ion could also be responsible for the observed 0.39 and 0.41-$\mu$m features. Golubeva et al. [1983] concluded that the surface mineralogy of Ceres was most likely dominated by hydrated nickel- and iron-rich silicates.

A more recent study published by Vilas and McFadden [1992] analyzed observations of Ceres taken on 7 April 1987 (UT). Weak absorption features were identified at 0.6 and 0.67 $\mu$m; however, these features were not correlated with those observed by Golubeva et al. [1983]. It was concluded by Vilas and Gaffey [1989] that these features were evidence for the presence of minerals created by aqueous alteration, but that the shallowness of the features precluded the possibility of significantly iron-bearing phyllosilicates (mineral products of aqueous alteration) as suggested by Golubeva et al. [1983]. The weak 0.6 and 0.67 $\mu$m absorption features were confirmed by Fornasier et al. [1999], but the 0.7 $\mu$m band seen in other Tholen G class asteroids was not observed.

In contrast to the hydrated features observed by Golubeva et al. [1983], Vilas and McFadden [1992], and Fornasier et al. [1999], more recent observations by Bus and Binzel [2002] as part of the SMASSII spectral classification program identify Ceres as a C-type asteroid with no observed 0.7 $\mu$m absorption feature characteristic of the presence of phyllosilicates. The SMASS survey identifies only a weak to moderate absorption at wavelengths shorter than 0.55 $\mu$m.

### 3.1.2 Variation in Surface Composition?

In the past decade, a number of different rotationally resolved studies of the surface of Ceres have been undertaken, beginning with a set of photometric surface maps taken

with the Hubble Space Telescope (HST) at UV and visible wavelengths [Li et al., 2006]. These maps observed albedo variations of only a few percent with a spatial resolution of 60 km, and it was concluded that the observed surface uniformity could be evidence of a resurfacing event since the period of heavy bombardment.

Subsequently, Carry et al. [2008] performed near-IR mapping of the surface in the J, H, and K bands with a spatial resolution of roughly 40-50 km. These near IR maps identified albedo features with diameters of 50-180 km and contrast of $\pm 6\%$, some of which were correlated with the features seen at visible wavelengths in the HST maps. The presence of similar features at many wavelengths suggests they are caused by geologic features of the surface.

Most recently, Rivkin and Volquardsen [2010] obtained rotationally resolved spectra of Ceres in the 2.2-4.0 $\mu$m range. Again, albedo variation as a function of longitude was measured to be $\pm 5\%$, similar to the results of Li et al. [2006] and Carry et al. [2008]. The 3 $\mu$m observations by Rivkin and Volquardsen [2010] also indicated slight variations (roughly 3%, only $1\sigma$ of the mean) in band depth that were found to be correlated with the features seen in Li et al. [2006] and Carry et al. [2008]. The weak variations were concluded not to be the result of significant changes in surface minerology, and it was suggested that variations in space weathering could be responsible for the result.

## 3.2 Observation of 1 Ceres on 2-5 January 2013 (UT)

Ceres was observed near close approach on 2-5 January 2013 (UT) using the DeVeny spectrograph on the Perkins 72-inch telescope at Lowell Observatory. These observations were made using the 300g/mm grating with wavelength coverage in the 0.43-0.85 $\mu$m range with a resolution of 2.2 $\AA$ per pixel. Observations of Ceres were alternated with observations of Hyades 64, a solar analog star, and HD35520, an A-type star for identifying telluric features. Sample raw data frames of Ceres and Hyades 64 can be

seen in Figure 3-1.

Spectra of Ceres were taken with 90 second exposures, except on the night of 3 January when 60s exposures were chosen to avoid saturation. On all nights the number of Ceres exposures taken consecutively was chosen to equal to 15 minutes of total exposure time. Observations of Hyades 64 were taken at 30 seconds on 2-3 January and the exposure time was increased to 45 seconds for 4-5 January to improve signal to noise. A total of 10 consecutive frames were taken of Hyades 64 at least once an hour. Because of its brightness, the exposure time for HD35520 was chosen to be 10 seconds. Ten consecutive frames of HD35520 were taken at a time (Table 3.1). Data for HD35520 are not tabulated as these data are not used in the analysis.

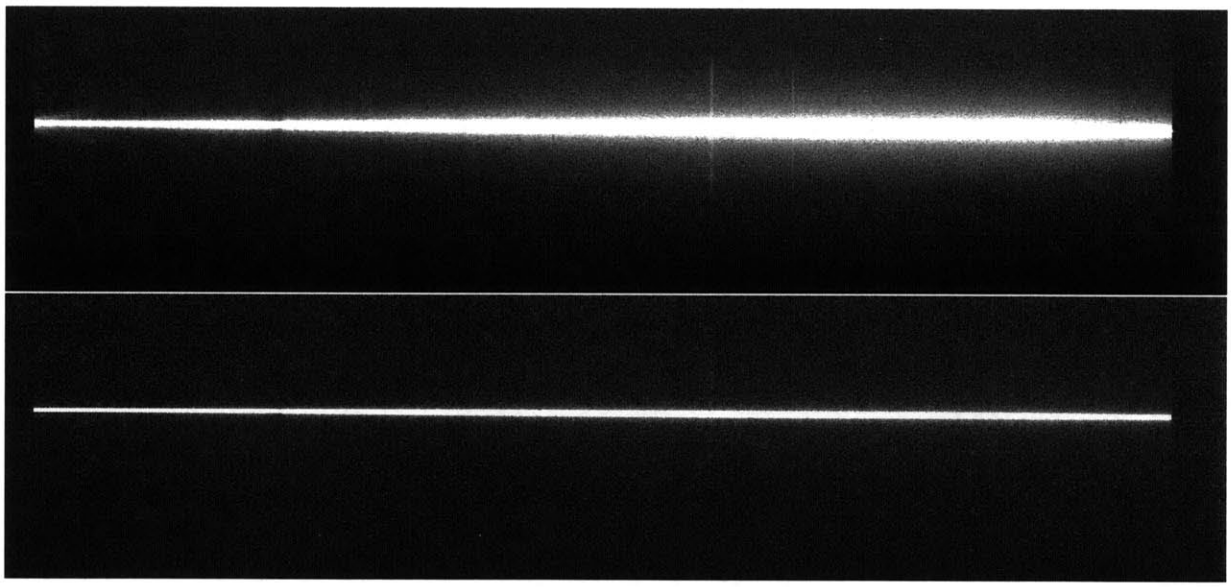

**FIGURE** 3-1: This figure shows raw data frames of Ceres (top) and Hyades 64 (bottom) on the night of 4 January 2013 (UT). Note that wavelength decreases to the right (bluer). The slit was 2.4". Along the y-axis the target is surrounded by sky, and two sky emission lines are visible in the Ceres sky background.

In addition to these science data, calibration images were taken each night consisting of 40 bias frames (20 at both the beginning and end of the night), 40 NeHgAr wavelength calibration frames (20 at the beginning and end of the night), and 20 flat field frames (taken only at the end of the night).

**TABLE** 3.1: Summary of data acquired during 2-5 January 2013 observations of Ceres.

| Date UT | Object | No. Frames | Exp (sec) |
|---|---|---|---|
| 1/2 | Ceres | 100 | 90 |
| 1/2 | Hyad 64 | 61 | 30 |
| 1/3 | Ceres | 184 | 60 |
| 1/3 | Hyad 64 | 100 | 30 |
| 1/4 | Ceres | 111 | 90 |
| 1/4 | Hyad 64 | 86 | 45 |
| 1/5 | Ceres | 144 | 90 |
| 1/5 | Hyad 64 | 126 | 45 |

## 3.3 Data Reduction

### 3.3.1 Reducing the Effects of Fringing

The chip on the DeVeny spectrograph exhibits significant fringing from roughly 0.78-0.85 $\mu$m. This fringing can be seen clearly in the flat field frame (Figure 3-2). While these effects were somewhat mitigated following normalization by the master flat for each night, there were still fringing effects visible in the extracted spectra. To further decrease the effects of fringing, a new set of flats were taken at each hour angle to account for changes in the fringe pattern as a function of telescope pointing. These new flats were used to reduce data frames taken at similar hour angle. This process helped to mitigate the worst effects; however, some fringing can still be seen in the final spectra at wavelengths longer than 7700 $\AA$ (Figure 3-4).

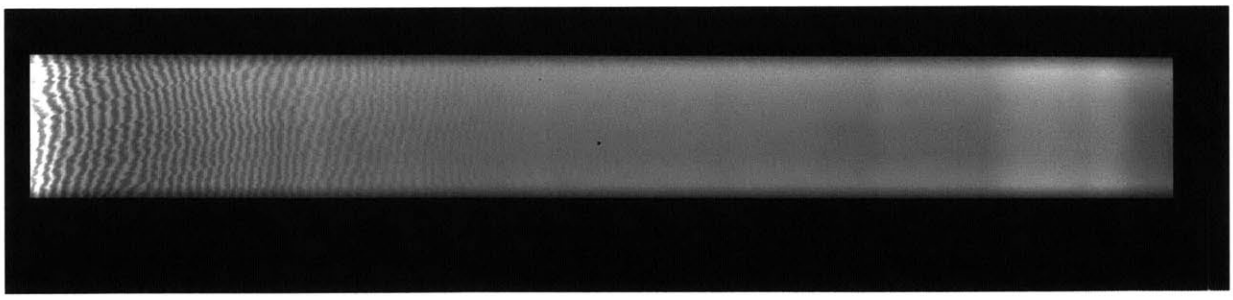

**FIGURE** 3-2: The master flat for observations on 4 January 2013. Notice the substantial fringing effects in the red (left) end of the chip.

### 3.3.2 Extracting Spectra

Spectra were extracted from the flattened data using a simple box extraction. A median sky value was calculated for each column and then subtracted from every pixel within the asteroid box. Column-wise summation within the asteroid box was then used to extract the raw spectrum. The broadening of the Ceres spectrum in the blue (Figure 3-1) necessitated the choice of a large extraction box so as not to exclude flux at shorter wavelengths. The same extraction box size was used for all data frames taken on all nights.

Sky apertures were chosen above and below the center of the asteroid aperture on the nights of 4-5 January. On the first two nights, the shutter froze open part-way through each night due to extremely cold temperatures, causing sky pixels to become contaminated with asteroid signal during chip read-out. Because the chip was read out from the bottom, only in rows above the Ceres spectrum was additional flux from Ceres collected during read-out. On these nights, sky was sampled only from the rows below the asteroid spectrum where pixels were uncontaminated. In frames taken with the shutter frozen open, the bottom sky aperture was increased to offset the loss of the upper sky sample.

The extracted Ceres spectra were then normalized by the Hyades 64 spectra to remove features inherent in the incident solar spectrum. For each night, the individual spectra were first averaged to find the mean spectrum during each set of consecutive exposures. Each mean Ceres spectrum was then normalized by the weighted average of the four Hyades 64 datasets nearest in airmass. Weights were determined using the difference in airmass between the Ceres and Hyades 64 datasets. The extracted spectra for the night of 5 January are shown in Figure 3-3.

### 3.3.3 Parallactic Angle Effects

Light traveling through the atmosphere undergoes dispersion as a function of wavelength. The parallactic angle is the angle along which this atmospheric dispersion occurs, and changes as a function of atmospheric thickness. The effect of atmospheric

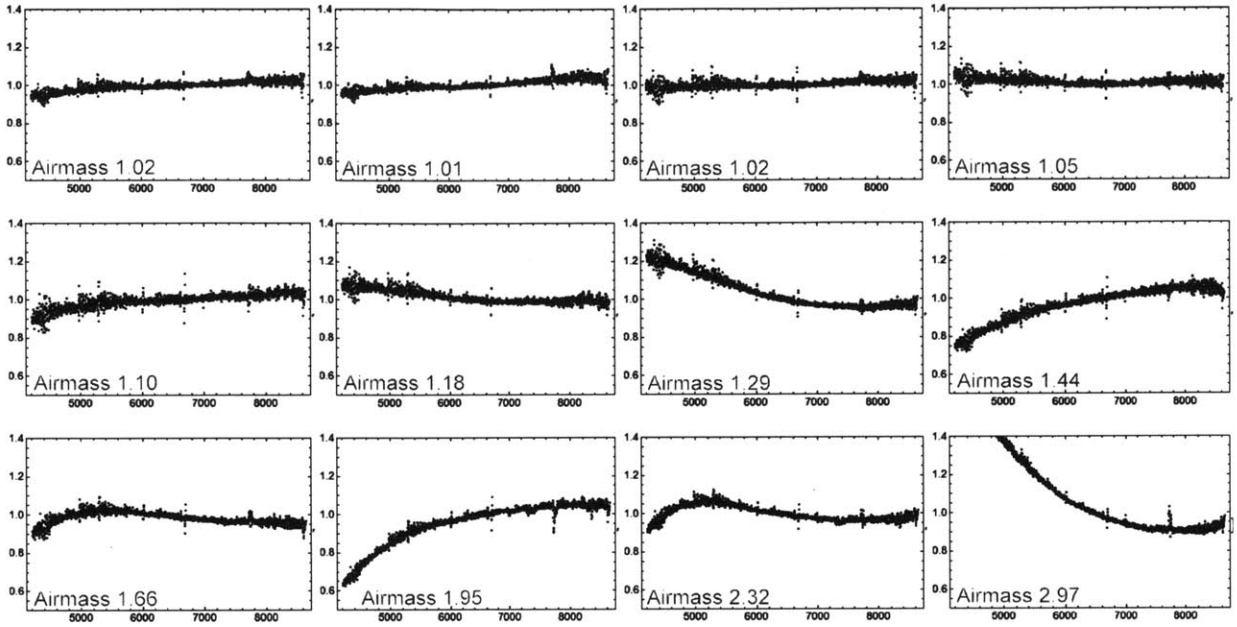


**FIGURE** 3-3: The complete set of calibrated Ceres spectra observed on the night of 5 January 2013. Each spectrum represents the average of 10 individual 90 second exposures. Airmass increases from left to right and from top to bottom.

dispersion is greater when observing over a large wavelength range. Even at small airmasses the changing parallactic angle can have a substantial effect on the shape of a spectrum across a large wavelength band. The effect is traditionally corrected for during data collection by rotating the slit into alignment with the parallactic angle as the object changes in airmass. Unfortunately, such rotation is unfeasible when using the DeVeny spectrograph on the Perkins telescope, so all data were taken at an angle of 0°. This angle matches the parallactic angle at 1.0 airmasses, but rapidly worsens as airmass increases. The variable slopes of the spectra apparent at high airmasses (Figure 3-3) are due to uncorrected parallactic angle effects.

An example of the magnitude of the effect of the parallactic angle from Filippenko [1982] shows that even at an airmass of 1.1 the offset between 3500 $\AA$ and 6500 $\AA$ is roughly 0.75 arcseconds. Since the Perkins data was taken with a slit width of 2.4 arcseconds, it was expected there would be substantial effects even at relatively small airmass. Using differential refraction as a function of airmass and wavelength at 7200 ft (the altitude of the Perkins) from Schleicher and Wagner [1985] and using the methods of Filippenko [1982], it was calculated that flux through the slit at 1.41

airmasses is 84% at 4500 $\AA$ and 78% at 9000 $\AA$. Because of this, data taken at airmasses greater than 1.3 have been excluded from the subsequent analysis.

### 3.3.4 Binning Spectra into Rotational Phase Bins

The phase of the data taken on different nights was computed using the mean exposure time in each exposure group and the rotational period of Ceres, 9.07417 hours [Chamberlain et al., 2007]. The zero phase was defined using midtime of the first set of Ceres exposures on 2 January 2013 UT, taken at 05:25 hours and corresponding to a sub-Earth longitude of 64°. Using this information, the data were divided into ten phase bins, each spanning 36° of longitude on Ceres. Spectra in the same bin were averaged together after normalization by the solar standard, resulting in 2-3 spectra being averaged together in most bins. A linear fit was used to remove the continuum slopes in the spectra to aid in the detection of shallow features. The spectra have also been binned to a resolution of 8.8 $\AA$ to improve the signal-to-noise ratio. The resulting mean spectrum in each phase bin is plotted in Figure 3-4.

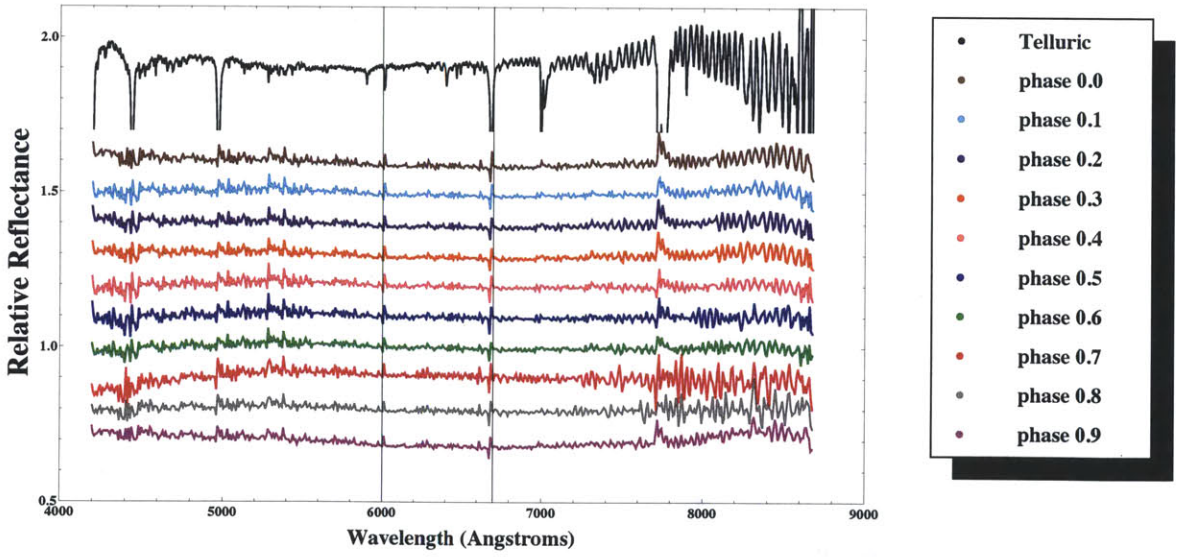


**FIGURE** 3-4: Calibrated Ceres spectra in ten phase bins are plotted on the same axes with artificial offsets. An A-star spectrum (black) is included to help identify uncorrected telluric features. Vertical lines are used to denote the 0.6 and 0.67 $\mu$m wavelengths where features have been seen in previous studies. No significant absorption features are apparent in the phased Ceres spectra.

To help identify subtle features that might not be visible in the phase-binned spectra, ratios taken between spectra at adjacent and at half-phase distances are plotted in Figure 3-5; however, no additional features are apparent in the ratioed spectra.

## 3.4 Discussion

### 3.4.1 Presence of the 0.6 and 0.67 $\mu$m Features

Shallow features seen in the Ceres spectrum at 0.6 and 0.67 $\mu$m have been reported previously [Vilas and McFadden, 1992, Fornasier et al., 1999]; however, in other studies [Bus and Binzel, 2002] these features were not seen. To quantify variation in these most recent spectra, the mean and standard deviation was computed across the 0.55-0.77 $\mu$m range for each of the 10 phase bins. Averages were computed in 300 $\AA$ bands centered on 0.6 and 0.67 $\mu$m were compared to the mean value found in the total 0.55-0.77 $\mu$m region. In these regions, any features correlated with features seen in the A-type star spectrum were removed prior to averaging. No 0.6 $\mu$m feature is seen but a 0.67 $\mu$m feature may be seen at roughly the 0.5% level; however, this variation cannot be viewed as statistically significant since it lies within the $1\sigma$ error (Table 3.2).

**TABLE** 3.2: Summary of spectral feature analysis.

| **Phase** | **Mean** | $\sigma$ | **0.6$\mu$m Ratio** | $\sigma$ | **0.67$\mu$m Ratio** | $\sigma$ |
|---|---|---|---|---|---|---|
| 0.0 | 0.986 | 0.008 | 0.995 | 0.012 | 0.991 | 0.013 |
| 0.1 | 0.996 | 0.010 | 0.998 | 0.014 | 0.995 | 0.017 |
| 0.2 | 1.005 | 0.014 | 1.003 | 0.019 | 0.998 | 0.024 |
| 0.3 | 0.999 | 0.008 | 1.001 | 0.013 | 0.994 | 0.012 |
| 0.4 | 0.999 | 0.008 | 1.000 | 0.015 | 0.996 | 0.013 |
| 0.5 | 0.999 | 0.008 | 1.000 | 0.014 | 0.995 | 0.012 |
| 0.6 | 0.994 | 0.008 | 0.997 | 0.013 | 0.993 | 0.012 |
| 0.7 | 0.995 | 0.008 | 0.996 | 0.013 | 0.993 | 0.012 |
| 0.8 | 0.995 | 0.007 | 0.998 | 0.012 | 0.994 | 0.011 |
| 0.9 | 0.990 | 0.008 | 0.996 | 0.013 | 0.991 | 0.014 |

### 3.4.2 Surface Variation

Previous studies of Ceres surface variation in the UV/visible [Li et al., 2006], and near-IR [Carry et al., 2008, Rivkin and Volquardsen, 2010] found the surface of Ceres to be remarkably uniform with surface variation of no more than 6%. In this study, no surface feature variation is seen at the 1% level, below the $1\sigma$ error level of $1-2\%$. The decrease in surface variation in these visible wavelengths compared ot previous results is perhaps to be expected given the general absence of features in the spectrum at visible wavelengths.

## 3.5 Conclusions

This study provides the first rotationally resolved spectra of Ceres in the 0.43-0.85 $\mu$m region with 36° resolution. These spectra show no variation with rotational phase at the 1% level, similar to previous work at other wavelengths [Li et al., 2006, Carry et al., 2008, Rivkin and Volquardsen, 2010], which concluded that the surface of Ceres is remarkably uniform. In addition, no statistically significant features are seen at either 0.6 or 0.67 $\mu$m in any phase bin, in agreement with the SMASS results [Bus and Binzel, 2002] but in disagreement with earlier work [Vilas and McFadden, 1992, Fornasier et al., 1999]. The broader 0.7 $\mu$m feature seen in many C-class asteroids is not seen in these spectra, in agreement with the results of the SMASS Survey [Bus and Binzel, 2002].

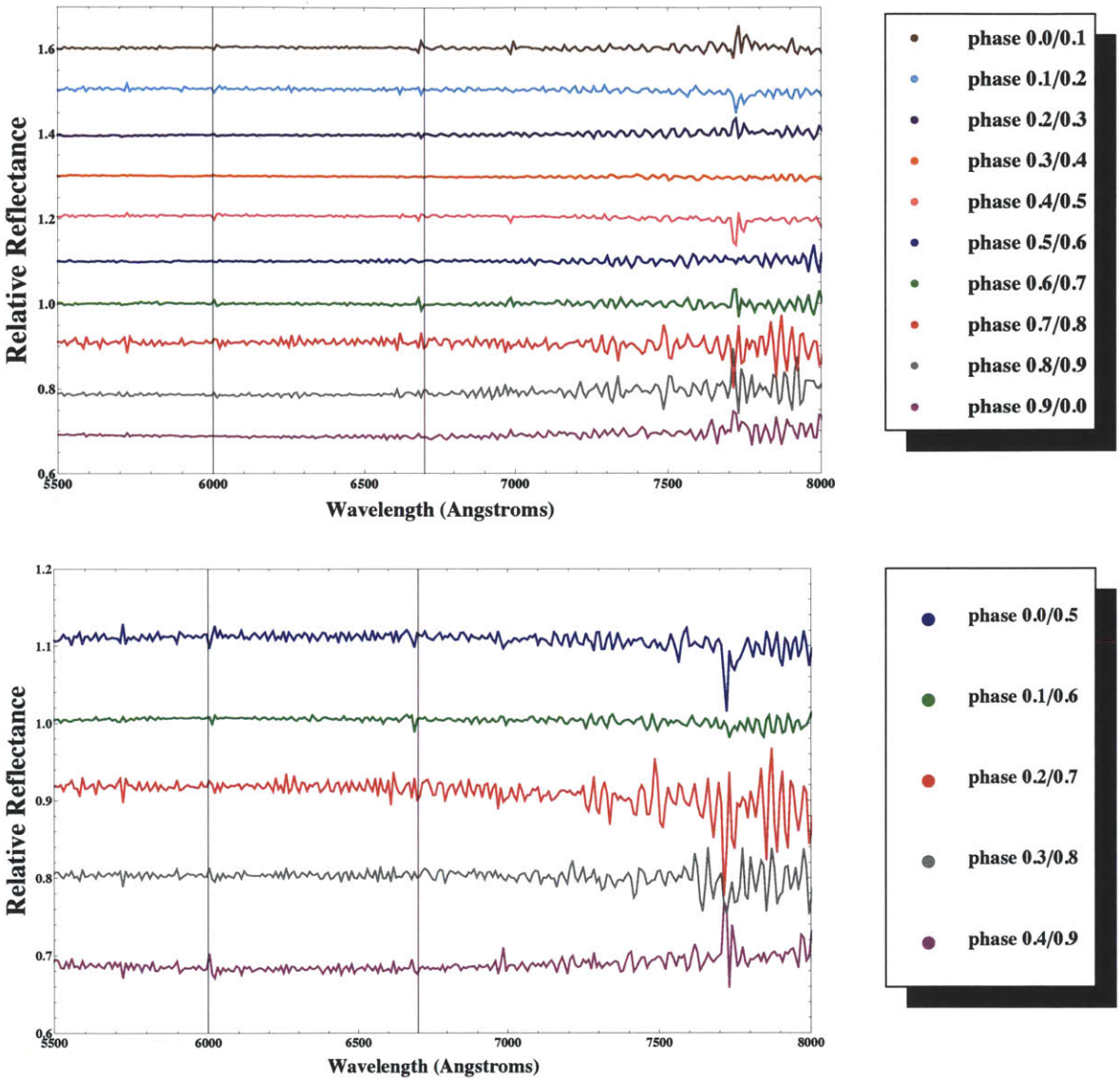


**FIGURE** 3-5: Ratios of spectra at different phase bins. Spectra have been trimmed to the 0.55-0.8 $\mu$m region to exclude the reddest and bluest regions which are most contaminated by fringing and parallactic angle effects. No evidence for additional features is seen. Top: Ratios of adjacent phase bins. Bottom: Ratios of opposite phases.

# Chapter 4

# Conclusions and Future Work

In this thesis two independent projects were undertaken. In the first, an occultation of 2060 Chiron was observed and the resulting data were used to constrain the radius of Chiron to 72-87 km. Additionally, twin symmetric absorption features were observed which exhibit near-circular symmetry, suggesting the presence of an arc or shell of dusty material located roughly 300 km from the body center and indicating that Chiron was active at the time of the occultation. Further study of Chiron using occultations could help to better constrain the presence of these features, depending on their variability as a function of time.

Additionally, the data presented in this document could be analyzed further were basic features of Chiron such as its density and rotation pole orientation better constrained. Without these it is impossible to accurately model the behavior of dusty material escaping from the nuclear surface and thus to leverage model fits as a technique for using occultation results to constrain jet geometry. Thus, better constraint of these basic properties would dramatically increase the utility of occultation observations in determining the morphology of observed jet-like features.

In the second project, rotationally resolved spectra of 1 Ceres were taken and analyzed for visible wavelength features as a function of rotational phase. The visible wavelength features seen in Vilas and McFadden [1992] and Fornasier et al. [1999] were not seen at any rotational phase. Furthermore, no spectral variation was seen as a function of phase at the 1% level. This result is in consistent with previous work at

other wavelengths which found variation at the level of only a few percent across the surface of Ceres [Li et al., 2006, Carry et al., 2008, Rivkin and Volquardsen, 2010].

The earliest studies of Ceres were performed more than 40 years ago, and since those early studies spectra have been observed in most wavelength bands. These spectral results point to a surface that is different from any known meteorite samples and is thought to be composed of minerals that are products of aqueous alteration. Despite extensive study, some controversy still exists as to the features seen in the visible wavelength spectrum and with regard to the correct interpretation of spectral features seen at other wavelengths. Nevertheless, the majority of scientific opinion continues to point toward evidence of minerals formed via processes of aqueous alteration. Due to the lack of significant surface variation it has also been suggested that Ceres has a remarkably uniform surface, and the slight variation has been suggested to be more likely due to differences in space weathering than actual compositional variation of the surface [Rivkin and Volquardsen, 2010]. It has even been suggested that the high degree of surface variation seen in the Ceres surface points to the possibility of a resurfacing event since the period of heavy bombardment [Li et al., 2006].

These questions will soon be answered with the arrival of Dawn at Ceres in 2015. After arrival, Dawn will gather imaging, spectral, and topographic data about the surface of Ceres [Rayman et al., 2006]. In addition to the surface studies, Dawn will also make precise measurements of the bulk density, rotation pole orientation, and gravitational field of Ceres. This detailed information will serve to further our understanding of planetesimal accretion in the early solar system and subsequent thermal evolution of Ceres.

# Bibliography

S. J. Bus and R. P. Binzel. Phase II of the Small Main-Belt Asteroid Spectroscopic Survey: A Feature-Based Taxonomy. *Icarus*, 158:146–177, 2002.

S. J. Bus, M. W. Buie, D. G. Schleicher, W. B. Hubbard, R. L. Marcialis, R. Hill, L. H. Wasserman, J. R. Spencer, R. L. Millis, O. G. Franz, A. S. Bosh, E. W. Dunham, C. H. Ford, J. W. Young, J. L. Elliott, R. Meserole, C. B. Olkin, S. W. McDonald, J. A. Foust, L. M. Sopata, and R. M. Bandyopadhyay. Stellar Occultation by 2060 Chiron. *Icarus*, 123:478–490, October 1996.

S. J. Bus, M. F. A'Hearn, E. Bowell, and S. A. Stern. (2060) Chiron: Evidence for Activity near Aphelion. *Icarus*, 150:94–103, March 2001.

B. Carry, C. Dumas, M. Fulchignoni, W. J. Merline, J. Berthier, D. Hestroffer, T. Fusco, and P. Tamblyn. Near-infrared mapping and physical properties of the dwarf-planet ceres. *A&A*, 478(1):235–244, 2008.

M. A. Chamberlain, M. V. Sykes, and G. A. Esquerdo. Ceres lightcurve analysis - Period determination. *Icarus*, 188:451–456, June 2007.

C. R. Chapman and J. W. Salisbury. Comparisons of meteorite and asteroid spectral reflectivities. *Icarus*, 19:507–522, August 1973.

J. L. Elliot, C. B. Olkin, E. W. Dunham, C. H. Ford, D. K. Gilmore, D. Kurtz, D. Lazzaro, D. M. Rank, P. Temi, R. M. Bandyopadhyay, J. Barroso, A. Barucci, A. S. Bosh, M. W. Bule, S. J. Bus, C. C. Dahn, D. W. Foryta, W. B. Hubbard, D. F. Lopes, R. L. Marcialis, S. W. McDonald, R. L. Millis, H. Reitsema, D. G. Schleicher, B. Sicardy, R. P. S. Stone, and L. H. Wasserman. Jet-like features near the nucleus of Chiron. *Nature*, 373:46–49, January 1995.

T. L. Farnham. Coma morphology of Jupiter-family comets. *Planetary and Space Science*, 57:1192–1217, 2009.

Y. R. Fernandez, D. Jewitt, and S. Sheppard. Thermal Properties of Centaurs Asbolus and Chiron. *AJ*, 123:1050, 1055, 2002.

A. V. Filippenko. The importance of atmospheric differential refraction in spectrophotmetry. *PASP*, 94:715, 721, August 1982.

S. Fornasier, M. Lazzarin, C. Barbieri, and M. A. Barucci. Spectroscopic comparison of aqueous altered asteroids with CM2 carbonaceous chondrite meteorites. *A&AS*, 135:65–73, February 1999.

M. Fulle. Spin axis orientation of 2060 Chiron from dust coma modeling. *Astron. Astrophys.*, 282:980–988, 1994.

L. F. Golubeva, S. Z. Omarov, and D. I. Shestopalov. Asteroid Symmetry. I. Surface Mineralogies of Ceres and Vesta. *Astron. Zh.*, 27:83–87, February 1983.

A. A. S. Gulbis, J. L. Elliot, F. E. Rojas, S. J. Bus, J. T. Rayner, W. E. Stahlberger, A. T. Tokunaga, E. R. Adams, and M. J. Person. A New Instrument for the IRTF: the MIT Optical Rapid Imaging System (MORIS). In *AAS/Division for Planetary Sciences Meeting Abstracts #42*, volume 42 of *Bulletin of the American Astronomical Society*, page 1005, October 2010.

D. Jewitt. The Active Centaurs. *AJ*, 137:4296–4312, May 2009.

T. V. V. King, R. N. Clark, W. M. Calvin, D. M. Sherman, and R. H. Brown. Evidence for ammonium-bearing minerals on Ceres. *Science*, 255:1551–1553, March 1992.

L. A. Lebofsky. Asteroid 1 Ceres - Evidence for water of hydration. *MNRAS*, 182: 17P–21P, February 1978.

L. A. Lebofsky, M. A. Feierberg, A. T. Tokunaga, H. P. Larson, and J. R. Johnson. The 1.7- to 4.2-micron spectrum of asteroid 1 ceres - evidence for structural water in clay minerals. *Icarus*, 48:453–459, December 1981.

J.-Y. Li, L. A. McFadden, J. W. Parker, E. F. Young, S. A. Stern, P. C. Thomas, C. T. Russell, and M. V. Sykes. Photometric analysis of 1 Ceres and surface mapping from HST observations. *Icarus*, 182:143–160, May 2006.

J. X. Luu and D. Jewitt. Cometary Activity in 2060 Chiron. *AJ*, 100:913–932, 1990.

T. B. McCord and M. J. Gaffey. Asteroids - Surface composition from reflection spectroscopy. *Science*, 186:352–355, October 1974.

K. J. Meech and M. J. S. Belton. The atmosphere of 2060 Chiron. *AJ*, 100:1323–1338, October 1990.

R. E. Milliken and A. S. Rivkin. Brucite and carbonate assemblages from altered olivine-rich materials on Ceres. *Nature Geoscience*, 2:258–261, April 2009.

D. Prialnik, N. Brosch, and D. Ianovici. Modelling the activity of 2060 Chiron. *MNRAS*, 276:1148–1154, October 1995.

M. D. Rayman, T. C. Fraschetti, C. A. Raymond, and C. T. Russell. Dawn: A mission in development for exploration of main belt asteroids Vesta and Ceres. *Acta Astronautica*, 58:605–616, June 2006.

J. T. Rayner, D. W. Toomey, P. M. Onaka, A. J. Denault, W. E. Stahlberger, W. D. Vacca, M. C. Cushing, and S. Wang. SpeX: A Medium-Resolution 0.8-5.5 Micron Spectrograph and Imager for the NASA Infrared Telescope Facility. *PASP*, 115: 362–382, March 2003.

A. S. Rivkin and E. L. Volquardsen. Rotationally-resolved spectra of Ceres in the 3-$\mu$m region. *Icarus*, 206:327–333, March 2010.

A. S. Rivkin, E. L. Volquardsen, and B. E. Clark. The surface composition of Ceres: Discovery of carbonates and iron-rich clays. *Icarus*, 185:563–567, December 2006.

D. G. Schleicher and T. L. Farnham. Photometry and imaging of the coma with narrowband filters. In M. H. Festou, U. Keller, and H. Weaver, editors, *Comets II*, pages 449–469. University of Arizona Press, Tucson, 2004.

D. G. Schleicher and R. M. Wagner. A guide to extinction and differential refraction. *IHW Newsletter*, 6:29–30, 1985.

S. A. Stern, A. A. Jackson, and D. C. Boice. Numerical simulations of particle orbits around 2060 Chiron. *AJ*, 107:765–771, February 1994.

F. Vilas and M. J. Gaffey. Phyllosilicate Absorption Features in Main-Belt and Outer-Belt Asteroid Reflectance Spectra. *Science*, 249:790–792, 1989.

F. Vilas and L. A. McFadden. CCD Reflectance Spectra of Selected Asteroids I. Presentation and Data Analysis Considerations. *Icarus*, 100:85–94, 1992.